PAPER

Check for updates

Unveiling the promoting mechanism of N-doping in porous biochar for formaldehyde adsorption: experimental and DFT studies

Ning Xiang,[a] Shaohua Wu, [b] Qingsong Zhao,[a] Yaqin Hou,*[c] Zhanggen Huang [*c] and Qiaoyan Li[d]

Nitrogen (N) doping in porous carbon adsorbents has been proven to be one of the effective strategies to enhance formaldehyde (HCHO) adsorption performance. However, the intrinsic promoting mechanism of specific nitrogen species (pyridinic-N, pyrrolic-N, and graphitic-N) remains unclear, hindering the rational design of porous carbon adsorbents. Herein, we prepared a series of nitrogen-doped porous biochars with alterable N species *via* one-step pyrolysis of urea and waste jujube pits in different proportions (BCU-*x*, *x* = 0–3), and the correlation between specific N species and HCHO adsorption performance was established for the first time. Experimental results show that the amount of surface pyrrolic-N (N-5) groups was the dominant factor in determining HCHO adsorption performance. Combined with DFT calculation results, it was revealed that the introduction of pyrrolic-N species significantly increased the inhomogeneity of electrostatic potential (ESP) distribution and the maximum absolute ESP value of carbonaceous models (increased from 15.94 kcal mol^{-1} to 50.15 kcal mol^{-1}) and consequently enhanced the affinity between polar HCHO and carbonaceous models (varied from −4.98 kcal mol^{-1} to −7.85 kcal mol^{-1}). Specifically, the O atom of HCHO tended to interact with the H atom attached to the pyrrolic-N moiety, and a hydrogen bond interaction (N–H⋯O=CH$_2$) existed. Therefore, the BCU-2 sample with the richest pyrrolic-N species exhibited the optimal HCHO adsorption capacity, of up to 21.25 mg g^{-1}, which was nearly 3.5 times higher than that of pristine biochar. This study clarifies the intrinsic promotion mechanism of specific nitrogen species in HCHO adsorption and provides general guidelines for the further design of high-performance carbonaceous adsorbents for HCHO removal.

1. Introduction

Over the past few years, indoor air pollution caused by formaldehyde (HCHO) has become a severe environmental problem threatening resident health.[1–3] Numerous studies have shown that long-term exposure to excessive levels of HCHO can cause severe skin/respiratory tract irritation, emphysema, and even acute leukemia.[4–6] Therefore, it is of great necessity to explore and develop highly effective, low-cost and environmentally friendly technologies for HCHO elimination. Physical adsorption is nowadays well-established as the optimal technology for HCHO removal, which shows the obvious advantages of reliability, safety and operation.[7,8]

As the common adsorbents, porous carbon materials have been widely used for HCHO removal owing to their well-developed pore structure, rich surface functional groups, and excellent chemical and thermal stability.[9–11] However, pristine porous carbon is generally non-polar or weakly polar, which is disadvantageous for the adsorption of polar HCHO molecules.[12] Ma *et al.*[13] reported that the HCHO breakthrough time of pristine coal-based activated carbon with a specific surface area of up to 1050 m^2 g^{-1} was less than 5 min, corresponding to an adsorption capacity of only 0.08 mg g^{-1}. In light of this, numerous efforts have been devoted to improving the HCHO adsorption performance of carbon-based adsorbents through various surface chemical modifications. Among these methods, heteroatom doping—particularly nitrogen (N) doping—has been proven to be one of the facile and efficient approaches to enhance HCHO adsorption performance.[14,15] de Falco *et al.*[16] suggested that N doping significantly improved the HCHO adsorption ability of wood-based activated carbon, which was attributed to the chemical/specific interaction between the introduced N-containing groups and HCHO. Similarly, Ryu *et al.*[17] found that N-rich chitin-derived activated carbon exhibited a HCHO adsorption capacity as high as 4.23 mg g^{-1}.

[a]Department of Life Sciences, Changzhi University, Changzhi 046011, PR China

[b]Academy of Environmental and Resource Sciences, School of Environmental Science and Engineering, Guangdong University of Petrochemical Technology, Maoming, 525000, PR China

[c]State Key Laboratory of Coal Conversion, Institute of Coal Chemistry, Chinese Academy of Sciences, Taiyuan 030001, PR China. E-mail: houyaqin@sxicc.ac.cn; zghuang@sxicc.ac.cn

[d]College of Environmental Science and Engineering, Taiyuan University of Technology, Jinzhong 030600, PR China

Although some studies have noted the promotion effect of N doping on HCHO adsorption, the intrinsic promotion mechanisms of specific N species (pyridinic-N, pyrrolic-N, graphitic-N, *etc.*) and the HCHO adsorption form are poorly documented. In particular, it is still ambiguous which N-functional group plays a key role in HCHO adsorption. Understanding the intrinsic promotion mechanisms of specific N species will definitely facilitate the design of porous carbon adsorbents for efficient HCHO removal.

The fabrication of carbonaceous materials with alterable N species is one of the prerequisites for studying the effects of specific N species. Benefitting from their flexible and adjustable chemical composition, low cost and widely available biomass, N-doped biochars (NBCs) have been widely studied and used for pollution remediation, energy storage, catalysis, and carbon sequestration in recent years.[18–21] Mian *et al.*[22] modulated the number and distribution of N-functional groups on sludge biochars by adding a different ratio of melamine and elucidated the correlation between specific N species and peroxymonosulfate activation. Chen *et al.*[23] prepared a series of edge-N-rich carbon nanosheet@porous biochars (NCN@PB) by adjusting cypress sawdust/melamine cyanurate ratios and found that pyrrolic N governed desulfurization activity owing to its fast H_2S dissociation and O_2 activation ability. The above results indicate that changing the doping ratio of the nitrogen source/biomass could adjust the number and distribution of specific N species and consequently allow us to establish a relationship between specific N species and HCHO adsorption performance. However, to the best of our knowledge, the application of N-doped biochar for HCHO adsorption, let alone the promoting mechanism of specific nitrogen functional groups, is relatively scarce.

In the present study, a series of N-doped jujube pit-derived biochars (BCU-*x*) with alterable N species were synthesized *via* one-step pyrolysis of urea and waste jujube pits in different proportions, where urea was used as a nitrogen source. With the help of multiple characterization methods and theoretical calculations, we comprehensively investigated and clarified the promoting mechanism of specific N-containing groups (pyridinic-N, pyrrolic-N, and graphitic-N) for HCHO adsorption. This study offers theoretical guidelines for the design of high-efficiency and green biochar adsorbents for HCHO removal.

2. Experimental

2.1. Materials

Jujube pits with the particle sizes between 20 and 40 mesh (0.45–0.90 mm) were obtained from the rural areas of Jining, Shandong Province. $ZnCl_2$ (99%), urea (99%) and formaldehyde solution (37 wt% in H_2O) were purchased from Macklin Ltd. HCl solution (36.0–38.0%) was purchased from Sinopharm Chemical Reagent Co., Ltd.

2.2. Preparation of biochars

First, 6 g jujube pit and different mass ratios of urea (urea/jujube pit mass ratios were 0, 1/1, 2/1 and 3/1) were mixed together. Subsequently, the blend was dispersed in 150 mL of ultrapure water containing 18 g $ZnCl_2$ and stirred at 80 °C for 5 h. The resulting samples were dried at 80 °C for 12 h and then activated at 600 °C (5 °C min^{-1}) for 2 h under a nitrogen atmosphere (150 mL min^{-1}). The activated samples were washed with 1.6 mol L^{-1} HCl solution three times, then washed to neutral with ultrapure water, and dried at 105 °C for 12 h. The obtained samples were labeled BCU-0, BCU-1, BCU-2 and BCU-3, respectively, based on the urea/jujube pit mass ratios.

2.3. Characterization, HCHO adsorption experiments and theoretical calculation methods

The details of the characterization, HCHO adsorption experiments and theoretical calculation methods are provided in the SI.

3. Results and discussion

3.1. Characteristics of the samples

The textural properties of the BCU-*x* samples were analyzed using N_2 sorption measurements. As shown in Fig. 1a, BCU-0 exhibited a combination of type I and IV isotherms. Specifically, a steep nitrogen uptake at a very low relative pressure (P/P_0 < 0.05) and a type-H4 hysteresis loop at a relative pressure of 0.4–0.7 were observed, which suggested the coexistence of micropores and mesopores. In contrast, these urea-modified biochars exhibited a classical type I-like isotherm.[24] With an increase in urea doping amount, the hysteresis loop gradually diminished. This indicates that urea doping decreased the amount of mesopores, which is in accordance with the pore size distribution (PSD) curves (Fig. 1b). The pore sizes of the BCU-*x* samples were mainly located in 0.5–2.0 nm. For the HCHO molecule, its diameter is only 0.25 nm. Therefore, these micropores of BCU-*x* samples should be enough for the diffusion and adsorption of the HCHO molecule.[25] As summarized in Table 1, the S_{BET}, V_{tot} and V_{micro} of the samples showed a decreasing trend with an increase in the urea doping amount, but the extent of the decline was markedly different. Compared with the pristine biochar BCU-0, the S_{BET} and V_{tot} of the N-doped biochars decreased by 31.88–54.04% and 45.54–66.41%, respectively. In contrast, the V_{micro} of the N-doped biochars decreased by only 3.19–36.53%. Meanwhile, the V_{micro}/V_{tot} ratios of the BCU-*x* samples gradually increased from 47.53% to 89.83% with an increase in the urea doping amount. This may be because urea integration blocked partial pores, leading to the conversion of some larger pores into micropores.[26]

The morphological features of the pristine biochar and N-doped biochar (represented by BCU-2) were investigated by SEM analysis. As shown in Fig. 2a and b, BCU-0 and BCU-2 exhibited similar morphology, which consisted of an irregular and porous massive structure. Additionally, the surface chemical composition and elemental distribution of BCU-0 and BCU-2 were examined by EDS mapping (Fig. 2c and d). For the BCU-0 sample, only C, O and sparse N element signals were observed. In contrast, BCU-2 demonstrated a significantly denser N
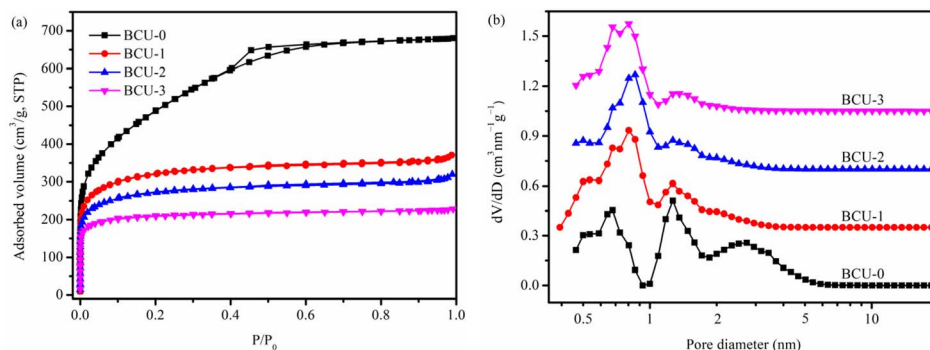
Fig. 1 (a) N₂ adsorption–desorption isotherms and (b) corresponding pore size distributions of BCU-0, BCU-1, BCU-2 and BCU-3.

Table 1 Textural parameters of BCU-0, BCU-1, BCU-2 and BCU-3

Sample	S_{BET} (m² g⁻¹)	S_{micro} (m² g⁻¹)	V_{tot} (cm³ g⁻¹)	V_{micro} (cm³ g⁻¹)	V_{micro}/V_{tot} (%)
BCU-0	1769	1031	1.054	0.501	47.53
BCU-1	1205	1138	0.574	0.485	84.49
BCU-2	1029	991	0.496	0.422	85.08
BCU-3	813	784	0.354	0.318	89.83

element distribution, which strongly confirmed the success of the N-doping strategy.

In order to characterize the crystal structure of the BCU-x samples, PXRD measurements were conducted. As shown in Fig. 3a, all the BCU-x samples exhibited two broad diffraction peaks centered around 2θ = 24–26° and 43°, corresponding to graphitic carbon (002) and (100) lattice planes, respectively.[24]

The broad diffraction peaks revealed the amorphous nature of the BCU-x samples.[27] Notably, the (002) lattice planes progressively shifted towards higher 2θ angles with an increase in the urea/jujube pit mass ratio. This might be because the introduction of nitrogen-containing moieties led to a gradually narrowed interlayer spacing.[28] In addition, the intensity of the

(100) plane gradually weakened with an increase in the urea/jujube pit mass ratio, demonstrating that the graphite phase of the BCU-x samples tended to weaken after urea modification. This could be because nitrogen doping introduced numerous heterocycles and defects into the carbonaceous skeleton and consequently destroyed the ordered structure of carbons.[29]

Fig. 3b depicts the Raman spectra of the BCU-x samples. The two conspicuous bands observed at 1335 and 1592 cm⁻¹ are attributed to the D-band and G-band, respectively.[30] For the undoped disordered carbons, the value of I_D/I_G primarily reflects sp² cluster size.[31,32] In contrast, for the N-doped carbons, the value of I_D/I_G mainly characterizes the defect degree of the materials. It is generally accepted that a higher I_D/I_G ratio indicates richer defect sites. As the urea/jujube pit mass ratio increased, the I_D/I_G ratios (based on peak heights) of the BCU-x samples gradually increased from 0.87 to 1.15, namely, a higher dose of nitrogen source contributed to richer defect sites, which was consistent with the XRD results (Fig. 3a).

XPS spectra were employed to reveal the effect of urea integration on the composition and chemical status of the biochar specimens. As shown in Fig. 4a, the signals located at 532, 399 and 285 eV were attributed to O 1s, N 1s and C 1s peaks, respectively.[33] The intensity of the N element was significantly increased after urea modification, further confirming the successful incorporation of N elements into the carbonaceous skeleton. Interestingly, the N atomic percentage of the samples (Table 2) first increased and then decreased as the urea/jujube pit mass ratio increased from 0 to 3. Moreover, BCU-2 exhibited the highest surface N atomic percentage (15.10 at%) among them. For BCU-3, its surface N atomic percentage decreased to 13.82 at%; meanwhile, its surface O atomic percentage increased to 13.27 at%. This demonstrates that an excess urea doping amount is unfavorable for increasing the surface N
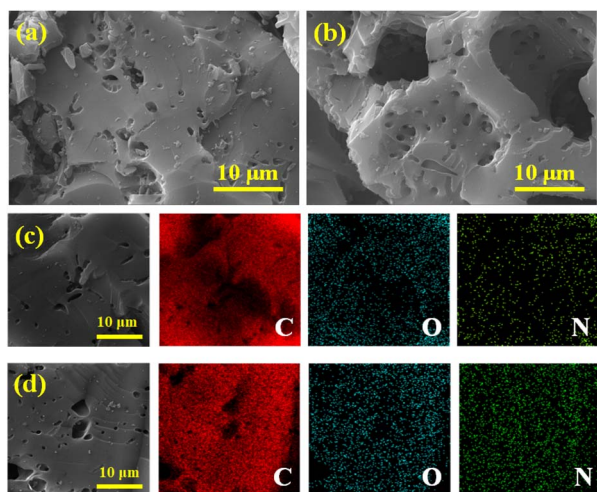

Fig. 2 SEM micrographs of (a) BCU-0 and (b) BCU-2. EDS elemental distribution of (c) BCU-0 and (d) BCU-2.
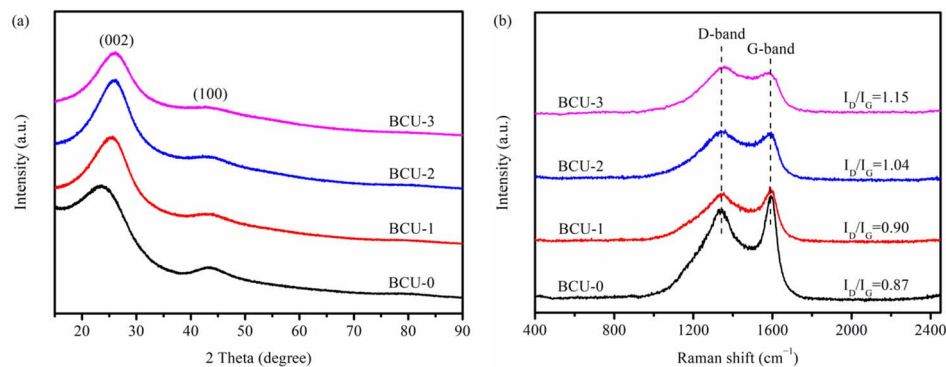
Fig. 3 (a) PXRD patterns and (b) Raman spectra of BCU-0, BCU-1, BCU-2 and BCU-3.
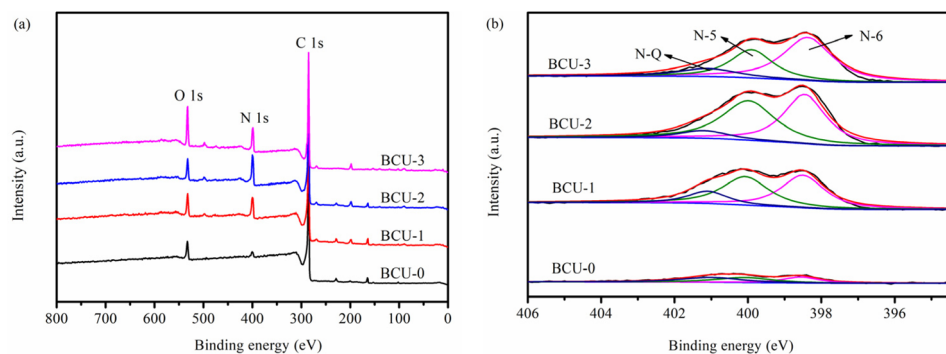

Fig. 4 (a) XPS wide scan and (b) N 1s scan of BCU-0, BCU-1, BCU-2 and BCU-3.

element content, which could be because the surface N elements were covered or substituted by oxygen elements derived from urea decomposition.

As shown in Fig. 4b and Table S1, the high-resolution N 1s spectra of the samples were deconvoluted into three peaks: 398.4 ± 0.2 eV for pyridinic-N (N-6), 400.0 ± 0.1 eV for pyrrolic-N (N-5), and 401.1 ± 0.1 eV for graphitic-N (N-Q).[34] Based on the surface total nitrogen content and relative ratio of each nitrogen-containing functional group, the overall content of each nitrogen-containing functional group was calculated, as summarized in Table 2. It could be observed that urea-induced nitrogen doping results in preferential introduction of edge-N species (*i.e.* pyrrolic N and pyridinic N), which could be because NH_3 derived from urea decomposition preferentially reacted with edge-C atoms or edge-oxygenated groups on the carbon framework.[35] Notably, the content of N-5 groups initially increased and then decreased with an increase in the urea/

jujube pit mass ratio. Moreover, BCU-2 exhibited the highest N-5 content among them. The N-6 content showed a gradually increasing trend. The content of N-Q varied slightly.

The high-resolution C 1s spectra of the samples are illustrated in Fig. S1a, which can be deconvolved into four independent components. The peak at 284.8 ± 0.1 eV was attributed to C–C (sp^2 hybridization). The peak centered at 286.0 ± 0.1 eV was ascribed to the carbon linked to nitrogen (C–N). The peak located at 287.2 ± 0.1 eV represents C–O. The peak situated at 289.0 ± 0.1 eV belonged to C=O.[29] As shown in Table S2, the C–N ratios of the samples initially increased and then decreased with an increase in the urea/jujube pit mass ratio, and BCU-2 demonstrated the highest C–N ratio, which is consistent with the trend of surface N content. The deconvoluted O 1s peaks (Fig. S1b and Table S3) indicated that oxygen species mainly existed in the form of C=O (531.5 eV), O=C–O (532.7 eV), and C–OH/C–O–C (533.6 eV).[36] No significant difference in the ratio of different O-containing species was observed (Table S3).

3.2. HCHO adsorption performance test

The HCHO adsorption capability of BCU-0, BCU-1, BCU-2 and BCU-3 was assessed using breakthrough curves. As shown in Fig. 5, BCU-0 demonstrated poor HCHO adsorption ability, which rapidly reached adsorption saturation. In contrast, the urea-modified biochar adsorbents showed a significant improvement in HCHO adsorption performance. With an
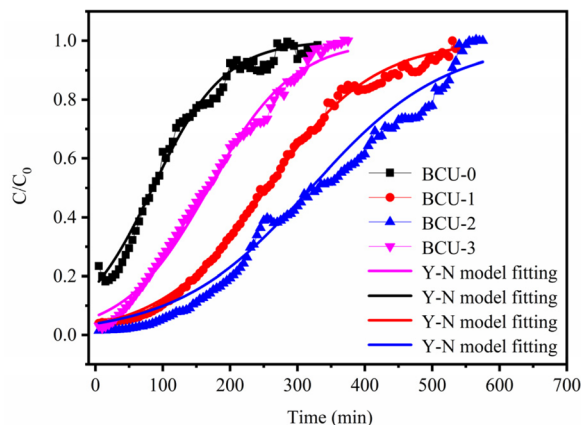
Table 2 Surface atomic percentage and overall content of specific nitrogen species in the samples

Sample	C (at%)	O (at%)	N (at%)	N-5 (at%)	N-6 (at%)	N-Q (at%)
BCU-0	90.97	6.02	3.19	1.14	0.87	1.18
BCU-1	82.42	6.77	10.81	4.43	4.74	1.64
BCU-2	78.20	6.70	15.10	6.93	6.93	1.24
BCU-3	72.91	13.27	13.82	4.32	7.78	1.72

Fig. 5 Dynamic HCHO adsorption breakthrough curves of BCU-0, BCU-1, BCU-2 and BCU-3.

increase in the urea/jujube pit mass ratio, the saturated HCHO adsorption capacity of the samples initially increased and then decreased. As presented in Table 3, the saturated HCHO adsorption capacity of the samples obeyed the following order: BCU-2 > BCU-1 > BCU-3 > BCU-0. These results suggest that moderate urea doping can effectively improve the saturated HCHO adsorption capacity of the BCU-x samples. Moreover, BCU-2 displayed optimal HCHO adsorption performance with a maximum adsorption capacity of 21.25 mg g^{-1}. It is also superior to that of many reported carbon-based adsorbents tested under similar conditions (Table S4).

In order to analyze the HCHO adsorption behaviors of the BCU-x samples, the breakthrough curves were fitted using the Yoon-Nelson model,[37] which can be expressed as follows:

$$t = T_{50} + \frac{1}{k}\ln\frac{C_t}{C_0 - C_t},$$

where T_{50} represents the required time when the outlet HCHO concentration reaches 50% of the inlet HCHO concentration, C_0 is the inlet HCHO concentration, C_t is the outlet HCHO concentration at t minute, and k represents the adsorption rate constant.

As shown in Fig. 5, the HCHO adsorption behavior of the BCU-x samples could be highly predicted using the Yoon-Nelson model, and their correlation R^2 values are above 0.975 (Table 3). The T_{50} initially increased and then decreased with an increase in urea/jujube pit mass ratio, which followed a similar trend with corresponding saturated adsorption capacity. The k

of these N-doped biochars was lower than that of pristine biochar, implying that N doping decreased the HCHO adsorption rate. This is likely due to partial pore blockage (especially mesopores) by the introduced surface moieties, which impeded the diffusion of HCHO. In addition, the HCHO breakthrough curves were fitted using the Thomas model (Fig. S2). As displayed in Table S5, the K_T of these N-doped biochars was also lower than that of pristine biochar, which further confirmed that N doping impeded the diffusion of HCHO.

In a real indoor environment, the relative humidity (RH) of air dramatically varies with the territory and climate. Therefore, it is of great importance to assess the influence of RH on the HCHO adsorption capacity of biochar. The corresponding saturated adsorption capacity of BCU-2 adsorbent at different RHs (10%, 35% and 60%) is shown in Fig. 6a. As the RH of the feed gas increased, the saturated adsorption capacity of BCU-2 gradually decreased. This was possibly because of the competitive adsorption between water vapor and HCHO.[38,39]

It is acknowledged that the regeneration and recycling of spent adsorbents could effectively reduce the cost of the HCHO adsorption process, which would promote the large-scale and practical application of HCHO adsorption technology. Five cycle tests of adsorption/regeneration were carried out over the spent BCU-2 (Fig. 6b). The saturated HCHO adsorption capacity of the BCU-2 adsorbent gradually decreased with an increase in regeneration times. To investigate the HCHO desorption behavior during the regeneration process, TPD measurement was conducted over the first saturated BCU-2. As displayed in Fig. S3, a well-defined HCHO desorption peak could be observed at 30–370 °C, corresponding to an HCHO desorption amount of 19.51 mg g^{-1}. This demonstrates that N$_2$ thermal purging at 400 °C is a feasible regeneration strategy. Compared with the fresh BCU-2 sample, the surface area and pore volume of spent BCU-2 significantly decreased after 5 adsorption/regeneration cycles (Table S6), which could be due to partial pore blockage by a fraction of the non-regenerable HCHO or its polymerization products. Consequently, saturated HCHO adsorption capacity of BCU-2 gradually decreased with an increase in adsorption/regeneration cycles. Nevertheless, the 5th regenerated BCU-2 retained 13.92 mg g^{-1} HCHO adsorption capacity, which was still significantly superior to that of fresh BCU-0 with 6.13 mg g^{-1} HCHO adsorption capacity. To sum up, BCU-2 has a promising application prospect for HCHO adsorption owing to its superb saturated adsorption capacity, recyclability and water resistance.

Generally, the HCHO adsorption capability of carbon adsorbents is primarily dependent on pore structures (such as specific surface area and pore volume) and surface functional groups. To evaluate the effect of the pore structures, the HCHO adsorption capacities of BCU-x samples were plotted against S_{BET}, S_{micro}, V_{tot} and V_{micro}. As shown in Fig. S4a–d, the relationship was not obvious. For example, pristine BCU-0 possesses the maximum S_{BET}, V_{tot}, and V_{micro}, but its HCHO adsorption capacity is the lowest among them. This demonstrates that the textural parameters of BCU-x should not be the dominant factors in determining HCHO adsorption capability and surface chemistry modifications can significantly outweigh

Table 3 Saturated HCHO adsorption amount and Yoon-Nelson model fitting parameters of BCU-0, BCU-1, BCU-2 and BCU-3

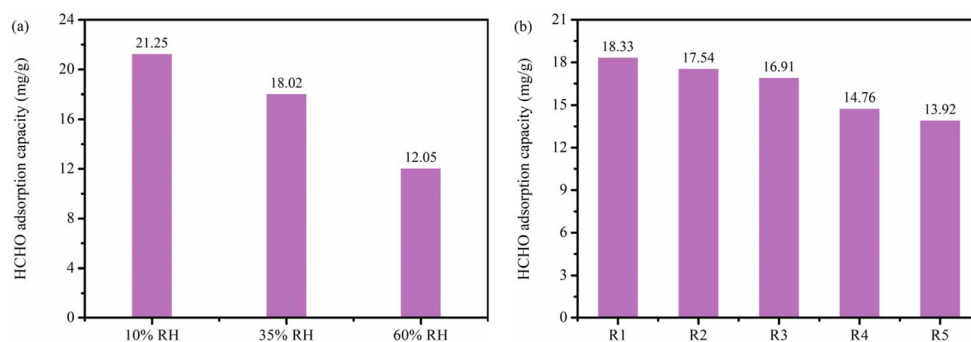| Sample	HCHO adsorption capacity (mg g^{-1})	T_{50} (min)	k ($\times 10^{-2}$ min^{-1})	R^2
BCU-0	6.13	85	1.88	0.986
BCU-1	16.56	255	1.27	0.997
BCU-2	21.25	320	1.00	0.975
BCU-3	10.75	165	1.60	0.992

Fig. 6 (a) Saturated HCHO adsorption capacity of BCU-2 at different relative humidities (10%, 35% and 60% RH); (b) saturated HCHO adsorption capacity of BCU-2 in five cycle tests.

the effects of surface area reduction. In addition, there was no obvious correlation between surface oxygen content, defects and HCHO adsorption capability (Fig. S5). Thus, it is reasonable to speculate that surface nitrogen-containing moieties could play a more important role during the HCHO adsorption process.

In order to assess the intrinsic effect of surface nitrogen-containing moieties on HCHO adsorption performance, the HCHO adsorption amounts of the BCU-x samples were normalized to the S_{BET}. The relationship between the normalized HCHO adsorption amount and the content of total N, N-5, N-6 and N-Q was plotted, as depicted in Fig. 7a–d. It is worth noting that an excellent correlation ($R^2 = 0.998$) was obtained between the normalized HCHO adsorption amount and the

content of the N-5 group. Meanwhile, as shown in Table S7, the correlation between the normalized HCHO adsorption amount and the N-5 content was statistically significant ($P < 0.05$). In contrast, the relationship between the normalized HCHO adsorption amount and the content of total N, N-6 or N-Q groups was not obvious. This implies that the enhanced HCHO adsorption performance was mainly attributed to the introduction of N-5 groups rather than total N or other N groups.

3.3. Computational simulation

According to the aforementioned experiment and analysis results, N doping, especially the N-5 group, could effectively
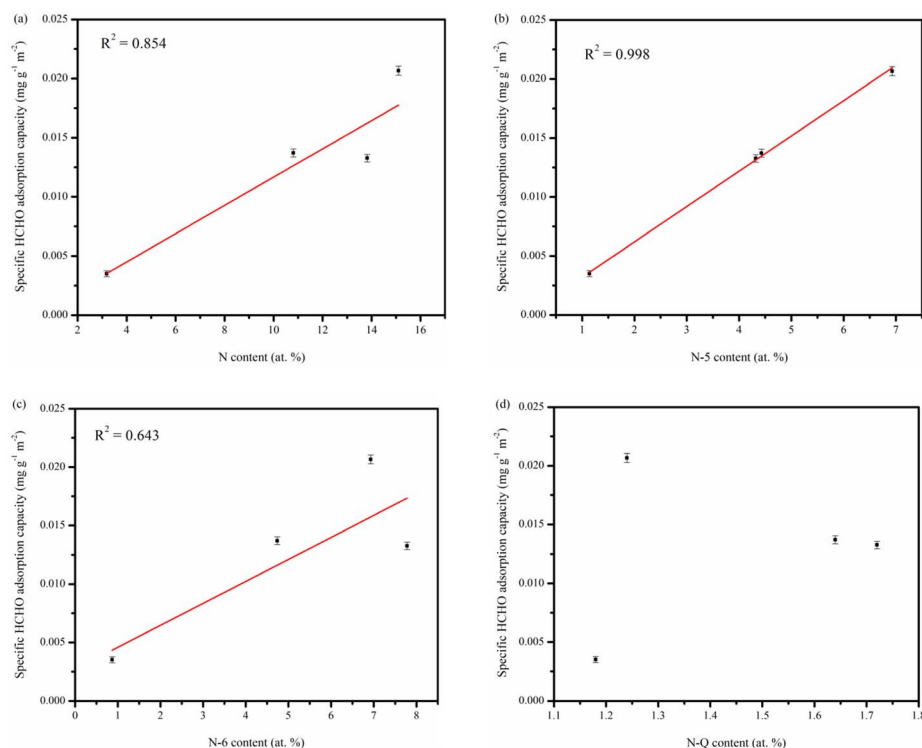

Fig. 7 Relationship between the normalized HCHO adsorption amount and the content of (a) total N, (b) N-5, (c) N-6 and (d) N-Q.

improve the HCHO adsorption capacity of the biochar adsorbent. However, because multiple nitrogen-containing moieties (N-5, N-6, and N-Q) coexist on the actual biochar, significant difficulties arise in determining the promoting mechanism of specific nitrogen-containing moieties for HCHO adsorption. Recently, theoretical calculations have been widely used to elucidate the intrinsic nature of surface interactions.[40–43] Herein, because of the complexity of nitrogen-containing moieties on the biochars, theoretical calculations were applied to investigate the interactions between HCHO and biochars with a specific nitrogen-containing moiety. Pyrrolic-N (N-5), pyridinic-N (N-6), and graphitic-N (N-Q) were chosen as the model nitrogenated groups based on the deconvolution results of the XPS spectra (Fig. 4b), and the corresponding carbonaceous models are shown in Fig. S6.

The electrostatic potential (ESP) analysis of targeted adsorbate and adsorbent models is vital for investigating and understanding intermolecular interactions and adsorption behaviors.[44] The regions with a negative ESP value are inclined to be attacked by electrophiles, while regions with a positive ESP value tend to serve as electron acceptors. The ESP distribution of the HCHO molecule is illustrated in Fig. 8a. As a typical polar molecule, HCHO exhibited a relatively wide and heterogeneous ESP distribution, ranging from -30.27 kcal mol^{-1} to 24.78 kcal mol^{-1}. The most negative global region $(-30.27$ kcal mol$^{-1})$ is located around the O atom, possibly resulting from the two lone-electron pairs and the large electronegativity of the O atom. Thus, the O atom with a highly negative ESP value was inclined to donate an electron. In comparison, the C atom and two H atoms manifested positive ESP values, demonstrating that the C atom and two H atoms were inclined to accept electrons. Thus, the most positive global region $(24.78$ kcal mol$^{-1})$ is located around the H atom due to the larger electronegativities of the O atom and C atom.

The ESP distributions of carbon sheets with or without a nitrogen-containing group are shown in Fig. 8b–e. For the perfect graphite (Fig. 8b), its ESP distribution was relatively uniform and narrow, ranging from -15.28 kcal mol^{-1} to 15.94 kcal mol^{-1}, which suggested that the perfect graphite was not able to form strong electrostatic interactions with the polar HCHO molecule. The basal surface of the benzene ring exhibited negative ESP values and could act as the electron donor, deriving from the π electron cloud.[45] The most positive global region $(15.94$ kcal mol$^{-1})$ is located around the H atom connected with the C atom of the benzene ring. Interestingly, the insertion of nitrogen-containing groups significantly remodeled the electron distributions of the carbon sheets. When the perfect graphite was decorated with the pyrrolic-N species (Fig. 8c), the local most positive region of ESP $(50.15$ kcal mol$^{-1})$ appeared near the H atom connected with the pyrrolic-N atom, which could serve as an electron acceptor. Since the N atom was more electronegative than the C atom and H atom, the vicinity of the pyrrolic-N atom manifested a relatively negative ESP value and could act as an electron donor. For pyridinic-N-doped graphite (Fig. 8d), the ESP value of the pyridinic-N atom was the global minimum $(-36.32$ kcal mol$^{-1})$, so the pyridinic-N atom would also serve as an electron donor. In the case of the graphitic-N-doped graphite (Fig. 8e), its ESP distribution ranged from -19.44 kcal mol^{-1} to 31.24 kcal mol^{-1}. The plane of the benzene ring and graphitic-N atom exhibited negative ESP values, while these H atoms located at the edge of the carbon sheet were positive. Overall, the above results demonstrated that the inhomogeneity of ESP distribution and the maximum absolute ESP value of carbonaceous models increased after N doping (especially pyrrolic-N doping). Based on the principle of electrostatic complementarity, it is reasonable to speculate that N doping (especially pyrrolic-N doping) should be advantageous to the adsorption of polar HCHO molecules, as further proved by the subsequent HCHO adsorption energy calculations.

The optimized HCHO adsorption structures of the original carbon sheet and the N-doped carbon sheets are shown in
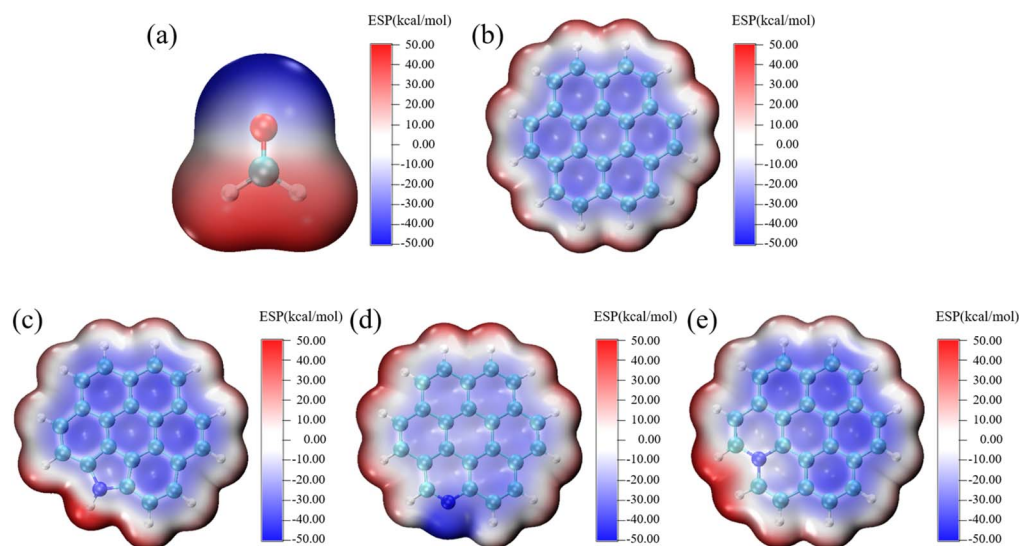

Fig. 8 ESP distributions of the HCHO molecule (a), carbon sheet models without an N atom (b), with pyrrolic-N (c), with pyridinic-N (d), and with graphitic-N (e).

Fig. 9a–d. In the case of the original carbon sheet (Fig. 9a), it was clear that the HCHO tended to basal plane adsorption. The electron-deficient C and H atoms of HCHO interacted with the plane of the benzene ring with π electron cloud, and the HCHO adsorption energy was -4.98 kcal mol^{-1}. For the carbon sheet model with pyrrolic-N (Fig. 9b), the O atom of HCHO was inclined to interact with the H atom linked to the pyrrolic-N moiety, and the corresponding physisorption energy was remarkably increased to -7.85 kcal mol^{-1}. This reveals that pyrrolic-N effectively enhanced HCHO physisorption, possibly owing to the hydrogen bond of N–H···O=CH$_2$. For the carbon sheet model with pyridinic-N (Fig. 9c), the HCHO was liable to adsorb on the edge site of the carbon sheet. There was an interaction between the H atom of HCHO and the pyridinic-N atom, corresponding to a physisorption energy of -5.38 kcal mol^{-1}. For the carbon sheet model with graphitic-N (Fig. 9d), it was obvious that HCHO was parallelly adsorbed on the basal plane of the benzene ring connected with the graphitic N atom, and the adsorption energy was -6.03 kcal mol^{-1}. The aforementioned results indicate that the HCHO physisorption energies over the N doping carbon sheets were higher than those of the raw carbon sheet model. Therefore, the introduction of pyrrolic-N species significantly increased the inhomogeneity of electrostatic potential (ESP) distribution and the maximum absolute ESP value of carbonaceous models (increased from 15.94 kcal mol^{-1} to 50.15 kcal mol^{-1}), and consequently enhanced the affinity between polar HCHO and carbonaceous models (varied from -4.98 kcal mol^{-1} to

-7.85 kcal mol^{-1}). Specifically, the O atom of HCHO tended to interact with the H atom attached to the pyrrolic-N moiety, and a hydrogen bond interaction (N–H···O=CH$_2$) existed. In addition, the effects of the N-6 and N-Q groups on HCHO adsorption were analyzed. Although the N-doped biochars also possessed rich N-6 species, the HCHO adsorption energy of the N-6-doped carbon sheet was only -5.38 kcal mol^{-1}, which was much lower than that of the N-5-doped carbon sheet (-7.85 kcal mol^{-1}). Thus, the relationship between the normalized HCHO adsorption amount and the content of the N-6 group was not obvious (Fig. 7c). The XPS results demonstrated that the N-Q content of the biochars varied slightly (Table 2); consequently, the significant difference in the normalized HCHO adsorption capacity should not be caused by the difference in the N-Q content (Fig. 7d). Based on the above analyses, BCU-2 with the highest pyrrolic-N content should exhibit superior HCHO adsorption performance, which is consistent with the experimental and DFT calculation results.

To verify the competition adsorption between HCHO and H$_2$O, the DFT calculation for H$_2$O adsorption on pristine carbon sheets and N-doped carbon sheets was also conducted. As shown in Fig. S7, the adsorption sites of H$_2$O on pristine carbon sheets and N-doped carbon sheets were similar to those of HCHO. Additionally, the H$_2$O physisorption energy on pristine carbon sheets and N-doped carbon sheets was close to their HCHO physisorption energy. The above results further validate the competitive adsorption between HCHO and H$_2$O.

4. Conclusions

In this study, a proof-of-concept investigation was carried out to explore the intrinsic promoting mechanism of specific nitrogen species of carbonaceous adsorbents on HCHO adsorption. Changing the doping ratios of the nitrogen source/biomass allowed us to adjust the number and distribution of specific N species and consequently establish the relationship between specific N species and HCHO adsorption performance. The experimental results identified that the amount of surface pyrrolic-N (N-5) group was the dominant factor in determining HCHO adsorption performance. Combined with DFT calculations, it was revealed that the introduction of pyrrolic-N species significantly increased the inhomogeneity of the electrostatic potential (ESP) distribution and the maximum absolute ESP value of carbonaceous models (increased from 15.94 kcal mol^{-1} to 50.15 kcal mol^{-1}) and consequently enhanced the affinity between polar HCHO and carbonaceous models (varied from -4.98 kcal mol^{-1} to -7.85 kcal mol^{-1}). In summary, this study not only clarifies the intrinsic promotion mechanism of specific nitrogen species in HCHO adsorption but also provides a fundamental guideline for the rational design and development of high-performance carbonaceous adsorbents for HCHO adsorption.
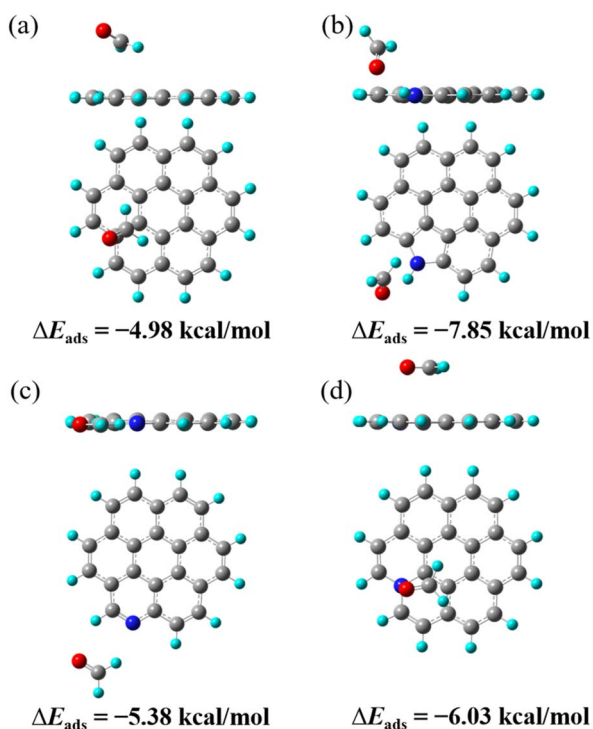

Fig. 9 Equilibrium HCHO physisorption configurations of carbon sheet models: (a) without an N atom, (b) with pyrrolic-N, (c) with pyridinic-N, and (d) with graphitic-N.

Author contributions

Ning Xiang: conceptualization, methodology, investigation, writing – original draft, funding acquisition. Shaohua Wu:

investigation, writing – review & editing. Qingsong Zhao: investigation, software. Yaqin Hou: writing – review & editing, project administration. Zhanggen Huang: writing – review & editing, project administration. Qiaoyan Li: visualization, and data curation.

Conflicts of interest

There are no conflicts to declare.

Data availability

Acknowledgements

References

1 T. Salthammer, S. Mentese and R. Marutzky, Chem. Rev., 2010, 110, 2536–2572.

2 X. Tang, Y. Bai, A. Duong, M. T. Smith, L. Li and L. Zhang, Environ. Int., 2009, 35, 1210–1224.

3 S. Q. Sun, K. Vikrant, S. Verma, D. W. Boukhvalov and K. H. Kim, J. Colloid Interface Sci., 2024, 653, 992–1005.

4 N. Xiang, Y. R. Bai, Q. Y. Li, X. J. Han, J. F. Zheng, Q. S. Zhao, Y. Q. Hou and Z. G. Huang, Mol. Catal., 2022, 528, 112519.

5 Z. Y. Di, R. D. Zhang, X. N. Guo, H. X. Shen, S. Royer, J. B. Jia, Y. Wei, Y. P. Li and L. R. Zheng, Fuel, 2025, 380, 133152.

6 J. Xie, Q. Y. Liu, C. H. Chen, T. Shen, X. Y. Tian, W. D. Shi and F. G. Wang, Fuel, 2025, 379, 133136.

7 K. J. Lee, J. Miyawaki, N. Shiratori, S. H. Yoon and J. Jang, J. Hazard. Mater., 2013, 260, 82–88.

8 J. W. Ye, X. F. Zhu, B. Cheng, J. G. Yu and C. J. Jiang, Environ. Sci. Technol. Lett., 2017, 4, 20–25.

9 W. C. Ji, M. P. Zhang, X. J. Fan, H. M. Zou, Y. Y. Meng, Y. B. Cai, F. D. Meng, H. Y. Wang and Y. Lou, Langmuir, 2023, 39, 11016–11027.

10 C. J. Na, M. J. Yoo, D. C. W. Tsang, H. W. Kim and K. H. Kim, J. Hazard. Mater., 2019, 366, 452–465.

11 S. Suresh and T. J. Bandosz, Carbon, 2018, 137, 207–221.

12 C. Q. Su, K. K. Liu, Y. Guo, H. L. Li, Z. Zeng and L. Q. Li, Surf. Interface Anal., 2021, 53, 330–339.

13 C. J. Ma, X. H. Li and T. L. Zhu, Carbon, 2011, 49, 2873–2875.

14 C. Q. Su, K. K. Liu, J. C. Zhu, H. Y. Chen, H. L. Li, Z. Zeng and L. Q. Li, Chem. Eng. J., 2020, 393, 124729.

15 Y. Song, W. Qiao, S. H. Yoon, I. Mochida, Q. Guo and L. Liu, J. Appl. Polym. Sci., 2007, 106, 2151–2157.

16 G. de Falco, W. L. Li, S. Cimino and T. J. Bandosz, Carbon, 2018, 138, 283–291.

17 D. Y. Ryu, D. W. Kim, Y. J. Kang, Y. Lee, K. Nakabayashi, J. Miyawaki, J. I. Park and S. H. Yoon, Carbon Lett., 2022, 32, 1473–1479.

18 S. H. Wu, Y. J. Zhao, R. R. Sun, Z. Q. Sun, C. P. Yang and J. Ma, Chem. Eng. J., 2025, 515, 163588.

19 Y. Z. Cheng, B. Y. Wang, J. M. Shen, P. W. Yan, J. Kang, W. Q. Wang, L. B. Bi, X. W. Zhu, Y. B. Li, S. Y. Wang, L. L. Shen and Z. L. Chen, J. Hazard. Mater., 2022, 432, 128757.

20 W. C. Ji, M. Z. Ren, H. F. Jin, Y. Lou, S. Z. Wang, X. J. Fan and S. Tabassum, Sep. Purif. Technol., 2025, 367, 132918.

21 J. Liao, K. Yin, X. D. Chen and B. C. Huang, New J. Chem., 2024, 48, 10273–10283.

22 M. M. Mian, G. J. Liu and H. H. Zhou, Sci. Total Environ., 2020, 744, 140862.

23 L. Chen, X. Jiang, S. G. Ma, W. H. Chen, B. Xu, Z. D. Dai, W. J. Jiang, Y. Peng and J. H. Li, Chem. Eng. J., 2023, 475, 146115.

24 J. Tian, X. X. Ding, Q. Wang, Y. T. Yang, S. Ma, Y. Q. Hou, Z. G. Huang and L. Liu, Sep. Purif. Technol., 2022, 301, 121809.

25 J. P. Bellat, I. Bezverkhyy, G. Weber, S. Royer, R. Averlant, J. M. Giraudon and J. F. Lamonier, J. Hazard. Mater., 2015, 300, 711–717.

26 Q. Y. Li, Y. Q. Hou, N. Xiang, Y. J. Liu and Z. G. Huang, Sci. Total Environ., 2020, 740, 140158.

27 F. Qi, J. B. Chen, Z. Q. Zeng, Z. G. Huang and Y. T. Niu, Chem. Eng. J., 2024, 499, 156077.

28 S. Liu, S. B. Wu and H. Cheng, Ind. Crops Prod., 2023, 192, 116120.

29 Q. Y. Li, Y. Q. Hou, J. C. Wang, Y. J. Liu, N. Xiang and Z. G. Huang, ACS Sustainable Chem. Eng., 2020, 8, 11308–11316.

30 S. H. Wu, Z. W. Yang, Z. Y. Zhou, X. Li, Y. Lin, J. J. Cheng and C. P. Yang, J. Hazard. Mater., 2023, 459, 132133.

31 A. C. Ferrari and J. Robertson, Phys. Rev. B, 2000, 61, 14095–14107.

32 X. Y. Liu, J. Choi, Z. Xu, C. P. Grey, S. Fleischmann and A. C. Forse, J. Am. Chem. Soc., 2024, 146, 30748–30752.

33 X. Y. Wang, M. A. Khan, M. Z. Xia, S. D. Zhu, W. Lei and F. Y. Wang, J. Mater. Sci.: Mater. Electron., 2019, 30, 5503–5515.

34 J. R. J. Zaeni, J. W. Lim, Z. H. Wang, D. H. Ding, Y. S. Chua, S. L. Ng and W. D. Oh, Sep. Purif. Technol., 2020, 241, 116702.

35 D. Li, W. H. Chen, J. P. Wu, C. Q. Jia and X. Jiang, J. Mater. Chem. A, 2020, 8, 24977–24995.

36 L. Qin, L. C. Wang, C. H. Wang, X. Yang and B. L. Lv, Mol. Catal., 2019, 462, 61–68.

37 X. X. Ding, Y. T. Yang, Z. Q. Zeng and Z. G. Huang, Environ. Sci. Technol., 2022, 56, 5786–5795.

38 N. Unglaube, M. Florent, T. Otto, M. Stötzer, J. Grothe, S. Kaskel and T. J. Bandosz, J. Colloid Interface Sci., 2024, 653, 594–605.

39 Z. H. Wang, Z. K. Sun, H. Q. Zhao, J. Li, X. Zhang, J. Y. Jia, K. B. An, Z. Y. Tang, M. Q. He and Z. B. Qu, *Sci. Total Environ.*, 2024, **910**, 168745.

40 X. Liu, J. Q. Liu, J. Y. Chen and F. C. Zhong, *J. Rare Earths*, 2023, **41**, 215–223.

41 Y. Y. Ge, C. Guo and C. Shi, *Sep. Sci. Technol.*, 2025, **60**, 1129–1138.

42 S. D. Zhu, H. H. Xu, M. S. Khan, M. Z. Xia, F. Y. Wang and Y. X. Chen, *Water Res.*, 2025, **272**, 122997.

43 Y. X. Chen, H. H. Xu, M. S. Khan, S. Q. Han and S. D. Zhu, *Crit. Rev. Environ. Sci. Technol.*, 2025, **55**, 1097–1123.

44 X. Zhu, L. Q. Zhang, M. Z. Zhang and C. Y. Ma, *Fuel*, 2019, **258**, 116109.

45 S. H. Zhang, Q. W. Chen, M. M. Hao, Y. Zhang, X. H. Ren, F. Cao, L. Zhang, Q. Sun and R. Wennersten, *Surf. Sci.*, 2023, **736**, 122352.